Structure–Property Relationships of Hyperbranched Polymer/ Kaolinite Nanocomposites

7 AUTHORS, INCLUDING:

Mona Abdel Rehim
National Research Center, Egypt

30 PUBLICATIONS   195 CITATIONS

SEE PROFILE

Andreas F Thünemann
Bundesanstalt für Materialforschung und -prü…

178 PUBLICATIONS   4,962 CITATIONS

SEE PROFILE

G. M. Turky
National Research Center, Egypt

46 PUBLICATIONS   338 CITATIONS

SEE PROFILE

A. Schönhals
Bundesanstalt für Materialforschung und -prü…

188 PUBLICATIONS   3,643 CITATIONS

SEE PROFILE

Macromolecules

Structure−Property Relationships of Hyperbranched Polymer/Kaolinite Nanocomposites

Shereen Shabaan Omara,[†,‡] Mona H. Abdel Rehim,[§] Ahmed Ghoneim,[‡] Sherif Madkour,[†] Andreas F. Thünemann,[†] Gamal Turky,[‡] and Andreas Schönhals[*,†]

[†]Bundesanstalt für Materialforschung und−prüfung (BAM), Unter den Eichen 87, 12205 Berlin, Germany

[‡]Microwave Physics and Dielectrics Department and [§]Packing and Packaging Materials Department, National Research Centre, 33 El Behooth St., Dokki, Giza, Egypt

ABSTRACT: Two methods were employed to prepare hyperbranched polyamine ester (HPAE)/kaolinite (Ka) nanocomposites resulting in different morphologies. In the case of the *in situ* polymerization, diethanolamine is inserted as monomer between the Ka layers and polymerized with methyl acrylate to prepare HPAE/Ka−DEA nanocomposites. For the *ex situ* method, Ka is modified with dodecylamine and solution-blended with HPAE. The former method leads to an intercalated morphology where the latter approach results in an exfoliated structure, as proofed by SAXS and TEM. A complementary combination of methods like differential scanning calorimetry (DSC), broadband dielectric relaxation (BDS), and specific heat spectroscopy (SHS) was used to investigate both kinds of nanocomposites in detail. Above T_g, the dielectric spectra are dominated by the conductivity contribution while the segmental dynamics is retrieved by SHS. A comparison of the temperature dependencies reveals a decoupling of segmental dynamics and conductivity, which becomes weaker with decreasing fragility.
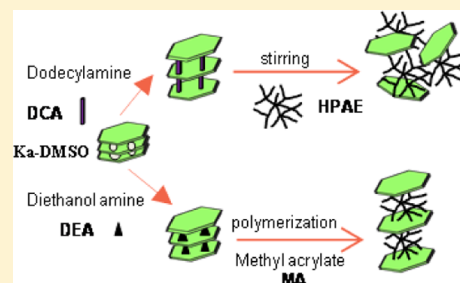
1. INTRODUCTION

Controlled macromolecular architecture has been recognized as an important tool to obtain polymers with tailored properties. Promising structures are hyperbranched polymers (HBPs). HBPs show the same unique potential as dendritic macromolecules such as low viscosity at a relatively high molecular weight, high solubility, miscibility, and high reactivity due to the large number of end groups, which can be also modified. However, HBPs have the further advantage being cost-efficient compared to dendrimers due to its one-step synthesis and no need of difficult purification steps. It has been also reported that the above-mentioned features of HBPs make them as promising materials for numerous applications, such as drug delivery systems, biosensors, coatings, etc.[1−4] Besides these applications, HBPs can be also used as advanced organic materials to prepare polymer based nanocomposites (see for instance refs 5−9).

Among the different polymer-based nanocomposite systems, the ones using layered silicates as nanofillers have the greatest interest because they can exhibit unique properties such as enhanced mechanical strength, improved thermal resistance, reduced gas permeability, etc. This makes them advantageous for various applications.[10−12] The most popular layered silicates with potential applications are montmorillonite (MMT), illite (hydro-mica), and kaolinite (Ka). Ka belongs to the group of nonswelling clay minerals with the chemical composition $Al_2Si_2O_5(OH)_4$.[13−15] However, because water molecules can hardly enter the interlayer space, Ka cannot be used to prepare nanocomposite materials by cationic ion exchange processes, like MMT. This is due to its poor hydration and unsatisfying mud-making ability. Nevertheless, different methods have been developed to prepare nanocomposites using Ka.[16,17] For instance, embedding polar organic molecules into Ka, before using it as nonfillers, will increase the distance between the Ka layers and consequently its hydration and mud-ability.[18]

To enhance the mechanical, electrical, and/or optical properties of HBP's, in many studies, different kinds of nanofillers were introduced to HBPs, yielding new nanocomposites with tailor-made properties. The properties of the final material can be adjusted as a function of the core structure, the degree of branching, and the type of functional end groups.[3] Furthermore, the method of the preparation of the nanostructures, the type of the nanofiller, and the treatment of its surface play an important role in preparing exfoliated or intercalated nanocomposites (see for instance refs 19−21).

The desire to prepare and to understand the properties HBPs and HBPs/nanocomposites has led to two major research branches. The first direction mainly focuses on the architecture of HBPs, their synthesis, and molecular characterization.[22−25] The second direction focuses on the understanding of the microscopic mechanisms responsible for the manifestation of their macroscopic properties.[26−28] Moreover, it addresses issues related to their detailed characterization, their ability to form a hydrogen-bonded network, and their structure−property relationship.[26] These points are also the focus of this work.

The molecular mobility of HBPs can be investigated by different methods like broadband dielectric spectroscopy. In principle, HBPs should show the typical relaxation processes known for glass-forming liquids, i.e., the α relaxation (segmental dynamics), related to the dynamic glass transition at temperatures above the thermal glass transition temperature, T_g, and secondary relaxations, originating from localized motions below T_g or at higher frequencies than that of the α relaxation. Turky et al.[27] investigated the influence of terminal groups on the dynamics of HBPs. It was found that at temperatures below T_g all studied systems exhibit a remarkably high charge carrier mobility and thus a high conductivity. In particular, for aliphatic hyperbranched polyureas the temperature dependence of the conductivity has been found to be of the Vogel–Fulcher–Tammann type.[29−31] It has been also reported[28] that the conductivity and the molecular dynamics of hyperbranched polyester do not follow a systematic dependence on the generation and therefore the number of terminal hydroxyl groups. This is due to their complicated architecture influenced by its intra- and intermolecular interactions. The dynamic glass transition and the conductivity were investigated for a family of hyperbranched polyesters in ref 4. The results revealed that there is a significant role of the hydrogen-bonded network on the segmental dynamics as well as a strong decoupling of the temperature dependence of the conductivity from that of the α relaxation.

For HBPs/nanocomposites, only few works considered the effect of the nanofillers on the molecular dynamics of the HBPs (see for instance refs 32 and 33). Recently, Androulaki et al.[33] reported a broadband dielectric spectroscopy study for three different generations of hyperbranched polyesters (Boltron) in the bulk and intercalated within MMT galleries. Compared to the bulk, the segmental motion under confinement changed substantially as it appears at temperatures below T_g of the bulk polymer with a changed temperature dependence. A corresponding behavior was observed for polymers confined to nanoporous glasses.[34,35] The β and γ relaxations became faster for the confined polymer compared to the bulk. Furthermore, a quasielastic neutron scattering study on hyperbranched polyester amide (Hybrane S 1200) and its nanocomposites with MMT by Fotiadou et al.[32] showed that for the polymer confined within the galleries (intercalated) the localized fluctuations have similarities to that of the bulk, whereas the segmental dynamics is completely suppressed.

In the past two decades, broadband dielectric spectroscopy (BDS) has been used to investigate the molecular dynamics of dendrimers[36−39] and HBPs.[40−43] Unfortunately, for the most HBPs, the α relaxation cannot or only hardly be observed by dielectric spectroscopy due to overlaying conductivity effects.[4,28] Like BDS, specific heat spectroscopy (SHS), for instance ac-chip calorimetry, is useful to investigate the dynamic glass transition[44−47] and is therefore a complementary method to BDS to investigate HBPs.

In this work, two different routes were used to prepare hyperbranched polyamine ester/kaolinite (HPAE/Ka) nanocomposites with different ratios of the filler. The so-called "ex situ" approach is a solution-based technique, where the prepared HPAE is mixed with Ka, which was previously modified by dodecylamine (DCA) to prepare HPAE/Ka−DCA nanocomposites. The "in situ" technique is a polymerization-based method. Here diethanolamine (DEA) is inserted as a monomer between the Ka layers and then polymerized with methyl acrylate to obtain HPAE/Ka−DEA nanocomposites.

The structure−property relationship of bulk HPAE and both types of nanocomposites were investigated by a combination of DSC, SAXS, FTIR, TEM, BDS, and ac-chip calorimetry.

2. EXPERIMENTAL SECTION

Materials. The natural Ka was supplied by Sinai Manganese Co., Egypt. Its chemical composition is $[Al_2Si_2O_5(OH)_4]$. Dimethyl sulfoxide (DMSO) $[(CH_3)_2SO]$, methanol (MeOH), diethanolamine (DEA) $[HN(CH_2CH_2OH)_2]$, dodecylamine (DCA) $[CH_3(CH_2)_{11}NH_2]$, and methyl acrylate (MA) $[CH_2CHCO_2CH_3]$ were purchased from Aldrich Chemicals.

Modification of the Kaolinite. *Intercalation of DCA into Kaolinite (Ka−DCA).* In the first step, kaolinite was modified by dispersing 1 g of Ka in 10 mL of DMSO and kept under continuous stirring (500 rpm) at room temperature for 3 days. The solution was filtered and washed with the same solvent, before drying at 323 K for 24 h. In the second step, the Ka−MeOH intercalated compound was prepared from the obtained product, as reported previously.[16] To replace the DMSO efficiently, the modified Ka product was dissolved in MeOH. The mixture was stirred at room temperature for 3 days, where the methanol was interchanged daily. The product was centrifuged, and a yellowish powder was obtained as Ka−DMSO−MeOH. As the last step, 1 g of prepared Ka−DMSO−MeOH precursor was added to 10 mL of DCA solution and continuously shaken in a closed flask for 5 days. Afterward, the dispersion was centrifuged, and the product was dried at 323 K for 24 h. Finally, a fine powder was obtained.[17]

Intercalation of DEA into Ka−DMSO (Ka−DEA). DEA was grafted to the interlayer aluminol groups of Ka by melt intercalation, using Ka−DMSO as starting material. 1 g of Ka−DMSO was dispersed in 6 g of the amino alcohol (DEA). The temperature of the mixture was then slowly increased from room temperature to 353 K and kept at 353 K for 48 h. The resulting nanohybrid material was recovered after three times of centrifugation and washing in 50 mL of isopropyl alcohol. Finally, the solid sample was dried at 333 K for 24 h.[18]

Preparation of HPAE/Ka Nanocomposites. *Preparation of Pure HPAE.* DEA was mixed with MA in the ratio of 1:1.2 using MeOH as solvent. The mixture was stirred continuously at room temperature for 48 h. The solvent was then removed under reduced pressure, using a rotary evaporator. The reaction was completed by keeping the mixture at 333 K for 1 h, at 373 K for 2 h, at 393 K for 2 h, and finally at 408−423 K for 2−4 h. After this temperature program, a yellow sticky polymer with a good solubility in water and methanol was obtained.[48] The molecular weight of the formed polymer was estimated using size exclusion chromatography [Agilent 1100 series with RI detection, using linear polystyrene as calibration standard, and N,N-dimethylformamide (DMF) as eluent]. The weight-average molecular weight (M_w), the number-average molecular weight (M_n), and the polydispersity index (PDI) = M_w/M_n of the prepared HP were estimated to 17 300 g mol^{-1}, 10 500 g mol^{-1}, and 1.6, respectively. The structure of HPAE, given in Figure 1, was characterized by ^{1}H NMR [NMR spectrometer Varian Mercury-Oxford 500 MZ, using DMSO-d_6 as solvent]. The polymer contains the expected three different kinds of OH groups: linear groups (N−CH$_2$−OH, δ = 3.5 ppm; N−CH$_2$−CH$_2$−OH), δ = 2.7 ppm), dendritic groups (CH$_2$−OCO, δ = 4.05 ppm; CH$_2$−N, δ = 3.4 ppm), and terminal groups (OH, δ = 4.48 ppm).

Preparation of HPAE/Ka by in Situ Polymerization. Ka−DEA was dispersed in methanol with different ratios by ultrasonicfiation for 24 h and added to DEA. MA dissolved in methanol was added to the previously prepared mixture in the ratio of 1:1.2. The obtained mixture was continuously stirred at room temperature for 48 h. The solvent was removed from the reaction system under reduced pressure using a rotary evaporator. The reaction temperature is increased to 333 K for 1 h and further followed by a temperature ramping: 373 K for 2 h, 393 K for 2 h, and finally 408−423 K for 2−4 h. After the completion of the reaction, a yellow sticky nanocomposite was obtained.

Preparation of HPAE/Ka−DCA by ex Situ Method. 0.5 and 1 g of Ka−DCA were dispersed in two different flasks containing water. 10 g
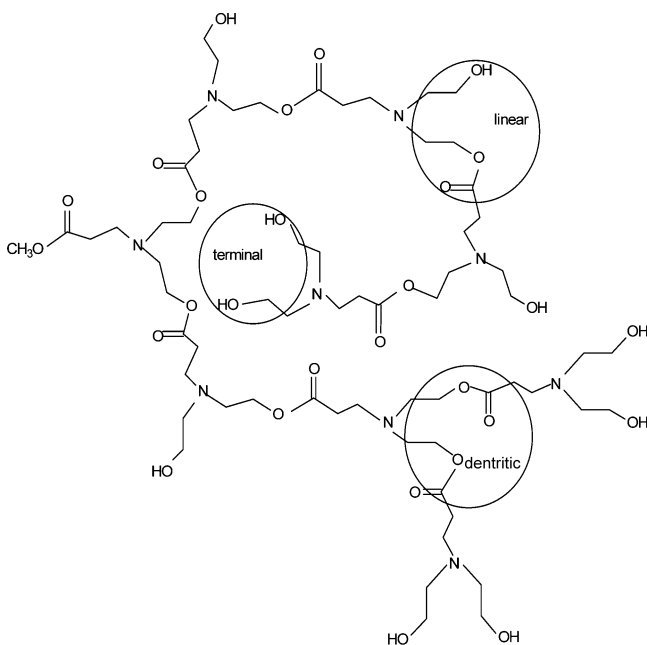
Figure 1. Structure of HPAE prepared by polycondensation of methyl acrylate and diethanolamine. Reproduced with permission from ref 48. Copyright 2011 John Wiley and Sons.

of HPAE dissolved in 100 mL of distilled H_2O was added to the solutions of Ka−DCA and kept under continuous stirring at 323 K for 2 days. In the last step, the solvent was removed from the system under reduced pressure using a rotary evaporator.[17] Figure 2 shows a scheme of the *in situ* and *ex situ* methods to prepare different types of HPAE/Ka nanocomposites.
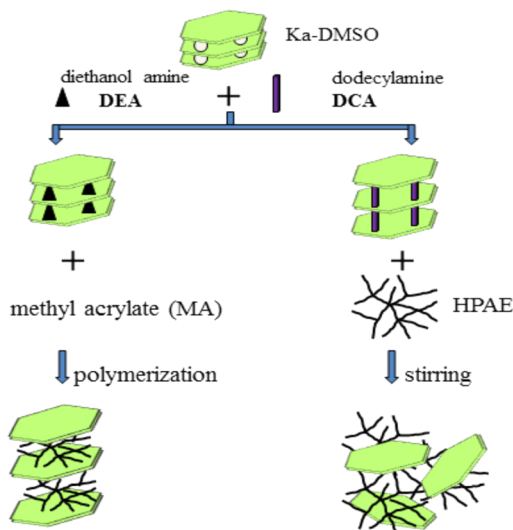
Figure 2. Scheme for the preparation of two different types of HPAE/Ka nanocomposites.

Characterization Techniques. *Fourier Transform Infrared Spectroscopy (FTIR).* The infrared spectra of the samples were measured in the wavenumber range from 550 to 4000 cm^{-1} accumulating 64 scans at a resolution of 4 cm^{-1} using a Nicolet Nexus 8700 FTIR spectrometer (Nicolet, USA) employing the ATR mode (Diamond Golden Gate, Nicolet, USA). All spectra were subjected to the ATR-correction for diamond, smoothed, and baseline corrected.

Small-Angle X-ray Scattering (SAXS). SAXS measurements were performed in a capillary with a Kratky-type instrument (SAXSess from

Anton Paar, Austria) at 298 ± 1 K. Each sample was measured for 180 × 10 s. The SAXSess has a low sample-to-detector distance (0.309 m), which is appropriate for investigation of samples with low scattering intensities. The measured intensity was corrected by subtracting the intensity of the empty capillary. The scattering vector is defined in terms of the scattering angle θ and the wavelength λ of the radiation (λ = 0.154 nm); thus $q = (4\pi/\lambda) \sin \theta$. Deconvolution (slit length desmearing) of the SAXS curves was performed with the SAXS-Quant software (Anton Paar, Austria).

Transmission Electron Microscope (TEM). Some morphological analyses were examined for dilute suspensions of corresponding nanocomposites in water, using a JEOL JEM-1230 TEM with an acceleration voltage of 80 keV. The probes of the nanocomposites were prepared by adding a small drop of the water dispersions onto a lacey carbon film-coated copper grid. Then grid was dried to constant weight first in air and second in high vacuum.

Broadband Dielectric Spectroscopy (BDS). The complex dielectric function $\varepsilon^*(f) - \varepsilon'(f) - i\varepsilon''(f)$ (ε' = real part, ε'' = loss or imaginary part, i = $\sqrt{-1}$, f − frequency) was measured by a high-resolution Alpha analyzer with an active sample head (Novocontrol GmbH, Germany) in the frequency range from 10^{-1} to 10^6 Hz and in the temperature interval from 173 to 323 K. The measurements were done isothermally where the temperature is controlled by a Quatro Novocontrol cryo-system with a stability of 0.1 K (for more details see ref 49).

The samples were prepared between two gold-plated stainless steel electrodes of 20 mm in diameter in parallel plate geometry. Fused silica fibers with a diameter of 50 μm were used as spacer.

Specific Heat Spectroscopy (SHS). SHS was employed using differential ac-chip calorimetry.[44] The calorimetric chip XEN 39390 (Xensor Integration, NI) was used as the measuring cell. The heater is located in the middle of a free-standing thin silicon nitride membrane (thickness 1 μm) supported by a Si frame with a window. This nanocalorimeter chip has a theoretical heated hot spot area of about 30 × 30 μm^2 with integrated 6-couple thermopiles and two four-wire heaters (bias and guard heater), as shown in ref 50. In addition to the 30 × 30 μm^2 hot spot, the heater strips also contribute to the heated area. The heaters and thermopiles are protected by a SiO_2 layer with a thickness of 0.5−1 μm.

In the differential approach to ac-chip calorimetry, the contribution of the heat capacity of the empty sensor to the measured signal is minimized. In the thin film approximation (submicron), the heat capacity of the sample C_S is then given by[44,45]

$$C_S = i\omega\overline{C}^2(\Delta U - \Delta U_0)/SP_0 \qquad (1)$$

where ω is the angular frequency ($\omega = 2\pi f$). $\overline{C} \equiv C_0 + G/i\omega$ describes the effective heat capacity of an empty sensor. S is the sensitivity of the thermopile, and P_0 is the applied heating power. ΔU is the complex differential thermopile signal for an empty reference sensor and a chip with a sample, where ΔU_0 is the complex differential voltage measured for two empty sensors. A more detailed description of the calorimetric chip, its differential setup, and the experimental method are given in ref 45. Absolute values of the heat capacity can be obtained by calibration procedures.[44]

For the calorimetric measurement, the temperature scan mode was used. The temperature was scanned using a heating/cooling rate of 2 K/min at fixed frequency. After each heating/cooling run the frequency was changed stepwise in the range of 1 Hz−10^4 Hz. The heating power for the modulation is kept constant at about 25 μW, which ensures that the amplitude of the temperature modulation is less than 0.5 K[45] and so a linear regime.

For the ac-chip calorimetry, empty sensors were first annealed for 2 h at 473 K in vacuum to completely cure the epoxy resin, which was used to glue the chip to the housing. Sensors were then mounted on a sample holder and placed under an optical microscope. A small drop of the HPAE or its nanocomposites (which were all in a viscous-liquid form at room temperature) was precisely placed on the heater area of the sensor, under the microscope.

Differential Scanning Calorimetry (DSC). Thermal analysis was carried out by DSC, Seiko Instruments DSC 220C. The samples (10 mg) were measured from 173 to 373 K with a heating/cooling rate of 10 K/min using nitrogen as protection gas. The glass transition temperature T_g was taken as the inflection point of the heat flow of the second heating run.

3. RESULTS AND DISCUSSION

Characterization of the Modified Ka. The inset of Figure 3 depicts a wide-angle X-ray scattering pattern for pure Ka. The
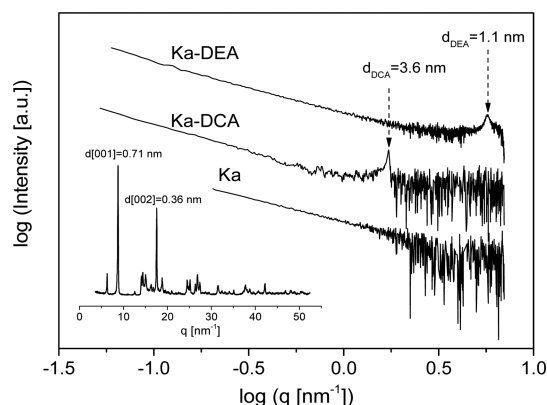
Figure 3. SAXS pattern of unmodified Ka, Ka−DCA, and Ka−DEA as indicated. The inset shows wide-angle X-ray data for pure Ka.

characteristic effective interlayer distance for Ka $d = 0.717$ nm ($q_{max} = 8.75$ nm^{-1}) corresponding to a laminar stack of Ka layers was observed in agreement with literature data.[14] By fitting a Gaussian to the data, the width w of the main peak is estimated. The correlation length in direction perpendicular to the lamella normal is $I_C = 2\pi/w = 72.6$ nm, and the effective number of layers is $I_C/d = 101$. Figure 3 shows the SAXS data of unmodified Ka, Ka modified by DCA, and Ka modified by DEA. For neat Ka no further reflections are detected in the SAXS range. For both modified Ka samples, the reflections are shifted to lower q values compared to the unmodified filler. The intercalation of DEA into Ka layers shows a reflection at $q_{max} = 5.71$ nm^{-1}; this value gives an effective interlayer distance of 1.12 nm. This means that the intercalation of DEA increases the effective interlayer distance compared to the pure Ka. The correlation lengths was estimated to be 20.3 nm; hence $I_C/d = 18$. The intercalation of the larger molecule of DCA increases the effective interlayer distance to 3.6 nm, also in agreement with literature data.[16] The correlation length was estimated to be 354 nm, and hence $I_C/d = 98$. As a result, comparing the I_C/d values for pure Ka and both modified Ka compounds, one has to conclude that the effective number of layers in the stack is quite low for Ka−DEA.

Figure 4a depicts the FTIR spectra of Ka, Ka−DCA, and Ka−DEA as an overview. The spectra are normalized by the intensity of the strongest peak. The spectra for the unmodified clay shows the characteristic vibrations expected for Ka: the OH stretching peaks (3620, 3650, 3668, and 3689 cm^{-1}) and the vibrations to the Si−O and Si−O−Si groups in the wavenumber range of ca. 1000 cm^{-1}. Figure 4b enlarges the spectra in the wavenumber range of the OH stretching vibrations. The peak at 3620 cm^{-1} is assigned to the inner OH groups were the other three peaks are related to the outer OH groups vibrations, at the surface of a Ka layer.[21,51] When DEA is intercalated into Ka, the characteristic peaks for OH
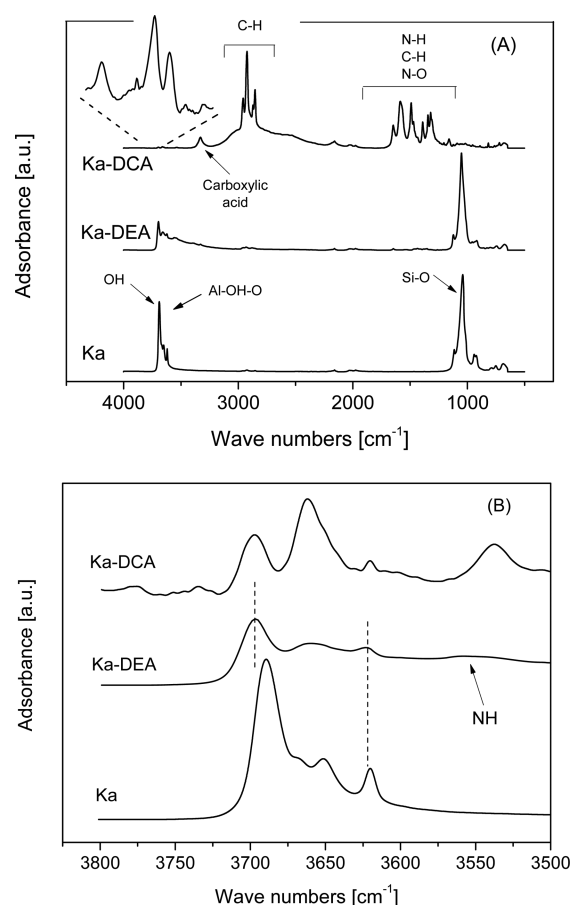

Figure 4. (A) FTIR spectra for Ka, Ka−DEA, and Ka−DCA. (B) FTIR spectra for Ka, Ka−DEA, and Ka−DCA in the wavenumber range from 3800 to 3500 cm^{-1}.

groups shifted to higher wavenumbers (3658 and 3696 cm^{-1}). This is related to the host−guest interaction by the hydrogen bonding. Moreover, the strong peak for Si−O−Si stretching vibration of pure Ka at 1041 cm^{-1} is shifted to higher frequency of 1051 cm^{-1} in Ka−DEA.[52] The additional peak at 3545 cm^{-1} is assigned to the NH stretching. This result also evidences the intercalating of DEA into Ka.

In the case of Ka−DCA, the vibrations of the OH groups are shifted to higher wavenumber like the case of Ka−DEA (see Figure 4b), which evidence grafting of DCA to the Ka layers. In addition, a slight shift in the peak of DCA at 1593 cm^{-1} to 1580 cm^{-1}, which is assigned to NH$_2$ bending mode, was observed. The splitting in the stretching vibration of CH$_2$ groups of DCA at 1466 cm^{-1} [53] to two peaks 1488 and 1468 cm^{-1} after intercalation confirms the formation of hydrogen bonds between DCA and the silica tetrahedron (see Figure 4a). Moreover, the splitting of the C−H stretching modes in the region of 2921 and 2853 cm^{-1} verifies that there is an interaction between the long alkyl chain of DCA and the Ka, in agreement with refs 54 and 55.

Characterization of HPAE Nanocomposites. Figure 5 shows FTIR spectra for pure HPAE and HPAE/Ka−DEA nanocomposites. The peaks are identified as follows. The broad peak for O−H stretching vibration, around 3380 cm^{-1}, evidences the presence of terminal hydroxyl groups in HPAE. The peaks at 2948 and 2883 cm^{-1} are due to the symmetric −CH$_3$ and asymmetric stretching −CH$_2$ vibrations. The absorption peaks at 1051 cm^{-1} is due to C−O stretching
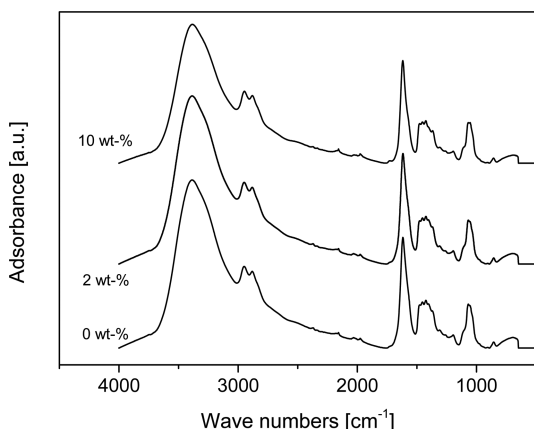
Figure 5. FTIR pattern for pure HPAE and HPAE/Ka−DEA nanocomposites (*in situ*) for 2 and 10 wt % of the filler. For sake of clearness the curves were shifted along the *y*-scale.

vibrations. The band at 1477 cm^{-1} corresponds to the bending vibration of −CH$_2$− groups. The sharp peak at 1620 cm^{-1} is related to N−H groups. It overlaps with the vibrations of the C=O groups, which were confirmed by NMR investigations for the bulk. This behavior was found for all *ex situ* and *in situ* samples and is consistent with the literature.[56] It is observed that the characteristic absorption peaks of the hydroxyl groups in the Ka−DEA at 3696 cm^{-1} disappeared in the spectra of HPAE/Ka−DEA. The location of this peak is usually sensitive to intercalation of organic molecules. For 2 and 10 wt % of Ka−DEA there are no major change in the chemical structural of the polymer polymerized in the presence of the nanofiller. Similar results were found in ref 57.

Figure 6 displays the SAXS patterns for HPAE/Ka−DEA (*in situ* preparation). Compared to the modified filler, no Bragg
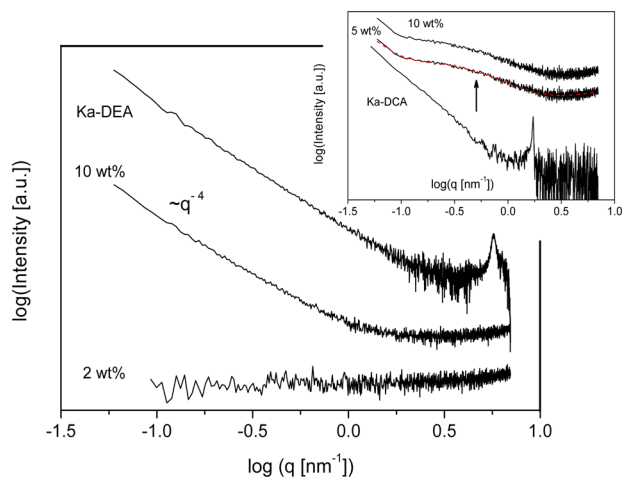

Figure 6. SAXS pattern for HPAE/Ka−DEA nanocomposites (*in situ*) for 2 and 10 wt %. The inset gives the SAXS pattern for HPAE/Ka−DCA nanocomposites (*ex situ*) for 5 and 10 wt % of the nanofiller.

peak is observed for the nanocomposites. First, in the low *q* range the data follow the Porod law ($I \sim q^4$) which indicates the existence of well-defined surfaces within the systems due to the presence of the nanoparticles (see the curve for 10 wt %). Second, for higher *q* values the *q* dependence of the scattered intensity is completely flat, which is due only to background contributions (see the curve for 2 wt %). There is no scattering

intensity which could be assigned to exfoliated objects like plates or disks, etc. This means the objects of the nanofiller in the sample must be larger than the scale defined by the *q* values of the SAXS experiment. The only interpretation that fits with these experimental results are stacks. The question arises why no Bragg peak is observed? To answer this question, one should keep in mind that already for modified Ka−DEA the observed Bragg peak is rather broad, much broader than for pure Ka and also for Ka−DCA. This indicates that already for Ka−DEA the layered structure is highly disturbed with strong lattice distortions. Furthermore, it is experimentally know that lattice distortions above 20% will lead to a disappearance of the corresponding Bragg peaks. From these results, it is concluded that in the case of *in situ* polymerization the nanofiller is organized in stacks. Because of the fact that also no Bragg reflections are observed, which are characteristic for the filler, it must be further concluded that these stacks have a highly disturbed structure with no long-range correlation. These findings are consistent with the TEM investigations (see Figure 6a). Thus, for the *in situ* prepared nanocomposites, it is concluded that they have a more or less intercalated structure.

The inset of Figure 6 depicts the SAXS patterns for HPAE/Ka−DCA (*ex situ* preparation). In this case also no Bragg reflection is detected, which is characteristic for the modified filler. In the *q*-range around 0.5 nm^{-1}, a broad scattering peak is detected for both concentrations of Ka−DCA. This pattern is attributed to the scattering of small aggregates consisting of rodlike structures. This is also in agreement with TEM investigations (see Figure 7b). Unfortunately, no structure
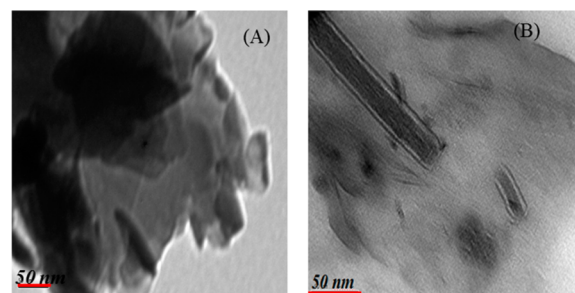

Figure 7. TEM pictures of the prepared nanocomposites for 10 wt % of the filler: (A) HPAE/Ka−DEA (*in situ*); (B) HPAE/Ka−DCA (*ex situ*). This size bar represents 50 nm.

factor could be found in the literature to describe the scattering data exactly. Therefore, a Lorentzian distribution is fitted to the data together with a Porod law and a background contribution. From the estimated position parameter of the distribution (5 wt %: 0.54 nm^{-1}; 10 wt %: 0.13 nm^{-1}) an average size of the objects can be estimated to 11.6 and 48.3 nm. The size is larger for 10 wt % of the nanofiller. Probably, the higher concentration of the nanofiller leads to larger aggregates. Form the SAXS and the TEM results; one has to conclude that the HPAE/Ka−DCA nanocomposites (*ex situ* preparation) have a predominated exfoliated structure (see Figure 2) in agreement with ref 17.

Figure 8 gives the DSC thermograms for HPAE/Ka−DEA. The thermal glass transition temperature T_g is estimated from the midpoint of the second heating run and given in Table 1.

In the case of *in situ* prepared samples, the T_g values for the samples with 2 and 10 wt % Ka−DEA are similar to that of pure
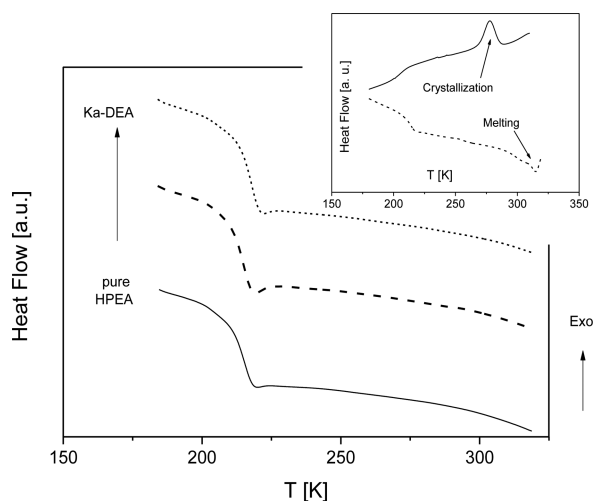
Figure 8. DSC thermograms for HPAE/Ka−DEA nanocomposites (10 K/min, second heating run): solid line, pure HPAE; dashed line, 2 wt % KA−DEA; dotted line, 10 wt % Ka−DEA. The inset shows the DSC thermograms of HPAE/Ka−DCA with 5 wt % of the filler. Solid line: cooling run after heating; dashed line: second heating (rate 10 K/min).

HPAE The absence of any other endothermic or exothermic peaks confirms that these nanocomposites are amorphous.[58]

The inset of Figure 8 gives the DSC thermograms of HPAE/Ka−DCA for 5 wt % of the nanofiller for heating and cooling. There is a slight decrease of T_g for both concentrations (see also Table 1). In addition to the glass transition, crystallization and melting peaks can be observed. Because of the fact that pure HPAE shows no phase transitions (see Figure 8), the melting and crystallization have to be attributed to DCA. Probably the long alkyl chains of DCA can and/or stimuli order like in alkenes. A similar behavior is found for 10 wt % of Ka−DCA. To avoid any influence of these crystallization phenomena on the specific heat and dielectric spectroscopy investigations, the highest temperature of the measurements was limited to 323 K (5 wt % Ka−DCA) or 333 K (10 wt % Ka−DCA).

To investigate the glass transition behavior in more detail, specific heat spectroscopy is employed using ac-chip calorimetry. According to eq 1, ac-chip calorimetry gives a complex differential voltage, which is related to complex heat capacity, as a function of temperature and frequency. Here the real part of the complex differential voltage U_R and the phase angle ϕ are taken as measures of complex heat capacity. At the dynamic glass transition, U_R increases stepwise with increasing temperature (Figure 9a), the phase angle shows a peak (Figure 9b). A dynamic glass transition temperature can be determined as the

half step temperature of U_R or as maximum temperature of the peak. In the raw data of the phase angle there is an underlying step in the signal, which is proportional to the real part. Hence, the phase angle must be corrected by subtracting this contribution.[44] This subtraction is in some way arbitrary. Therefore, here a different method is employed to estimate the dynamic glass transition temperature. The real part of U_R is differentiated with respect to temperature. This procedure also leads to a peak (see Figure 9c). A Gaussian is fitted to these data, and T_g is taken as the maximum temperature. Together with the frequency the relaxation map can be constructed (see Figure 10).

For the following discussion it should be noted that the experimental error of an ac-chip calorimetry measurement is 2−3 K. For pure HPAE, the temperature dependence of the relaxation rate $f_{p,\alpha}$ is curved when plotted versus $1/T$ as expected for the dynamic glass transition. The data can be described by Vogel−Fulcher−Tammann (VFT) equation[29−31]

$$\log f_{p,\alpha} = \log f_\infty - \left(\frac{A}{T - T_0}\right) = \log f_\infty - \left(\frac{D T_0}{T - T_0}\right)$$

(2)

where f_∞ and A are fitting parameters and T_0 is called ideal glass transition or Vogel temperature, which is found empirically to be 30−70 K below the thermal T_g. The parameter $D = A/T_0$ is called fragility parameter (fragility strengths) and provides among others a useful quantity to classify glass forming systems.[59,60] Materials are called "fragile" if their $f_{p,\alpha}(T)$ dependence deviates strongly from an Arrhenius-type behavior and "strong" if $f_{p,\alpha}(T)$ is close to the latter.

For the HPAE/Ka−DEA (*in situ*) nanocomposites with 2 and 10 wt % nanofiller, the temperature dependence of $f_{p,\alpha}$ is located in the same temperature region as that of pure HPAE. However, a closer inspection of the data reveals that there are systematic deviations of the temperature dependence of $f_{p,\alpha}(T)$ for the Ka−DEA nanocomposites from that of pure HPAE. For the lowest measuring frequency the observed differences are significantly larger than the error of ac-chip calorimetry. Moreover, the whole temperature dependence changes from a fragile to a more strong behavior. This is also seen from the calculated fragility parameter (see Table 1). The observed relaxation map is expected for a confined material.[35]

The data for the HPAE/Ka−DCA nanocomposites are given in the inset for Figure 10. Also for this set of samples the data for the nanocomposite deviate substantial from that of pure HPAE. The VFT dependencies for the nanocomposites show a much stronger behavior than that of pure HPAE.

Close and above the thermal glass transition the dielectric behavior of HBPs is dominated by high conductivity contributions.[4,61] Therefore, the segmental motion related to

Table 1. Glass Transition Temperature T_g (Second Heating), VFT Parameters Estimated from Specific Heat Spectroscopy, Fragility Parameter D for the α Relaxation for Pure HPAE and Its Nanocomposites, and Activation Parameters for the γ Relaxation

	sample	α relaxation (specific heat spectroscopy)					γ relaxation	
		T_g [K]	$\log(f_\infty$ [Hz])	A [K]	T_0 [K]	D	$\log(f_\infty$ [Hz])	$E_{A,\gamma}$ [kJ/mol]
	pure HPAE	220	12	497.6	198.9	2.5	12.2	31
in situ	2 wt %	219	12	608.7	176.8	3.4	11.3	28
	10 wt %	222	12	756.6	160.1	4.7	13.1	33
ex situ	5 wt %	213	12	843.4	155.5	5.4	10.2	24
	10 wt %	216	12	917.6	148.3	6.2	11.2	26
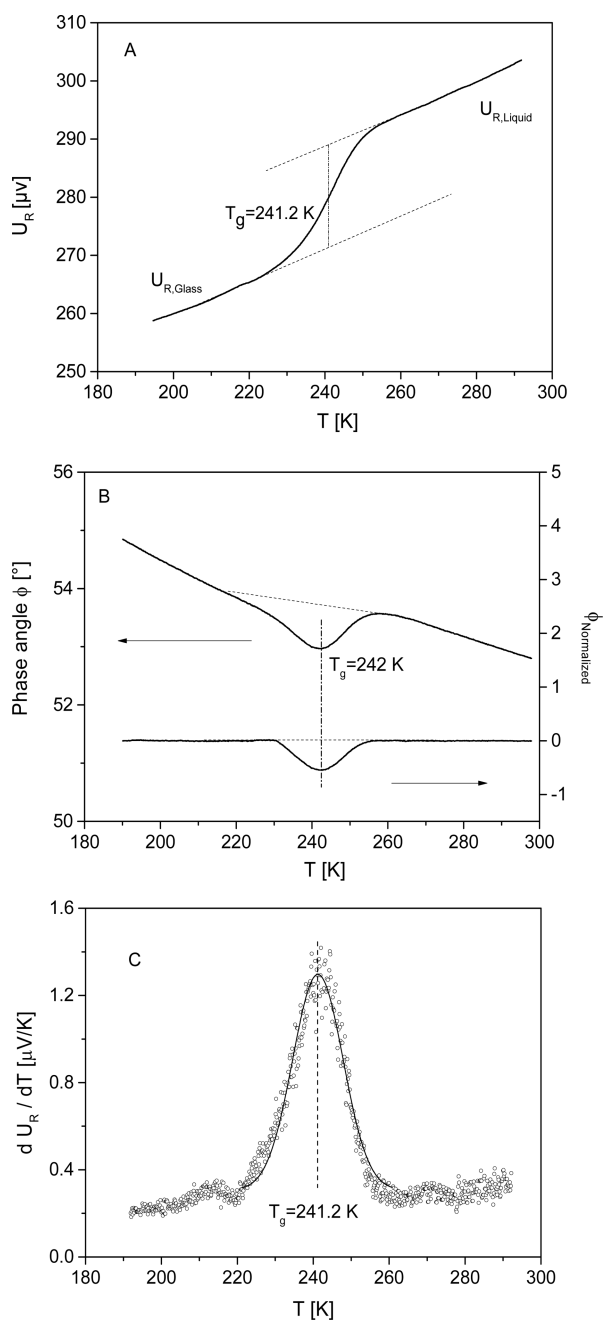
Figure 9. Example for an ac-chip calorimetry measurement for pure HPAE at a frequency of 160 Hz. (A) Real part of the complex differential voltage versus temperature. (B) Phase angle and corrected phase angle versus temperature. (C) Derivative of the real part of the complex differential voltage versus temperature. The line is a fit of a Gaussian to the data.
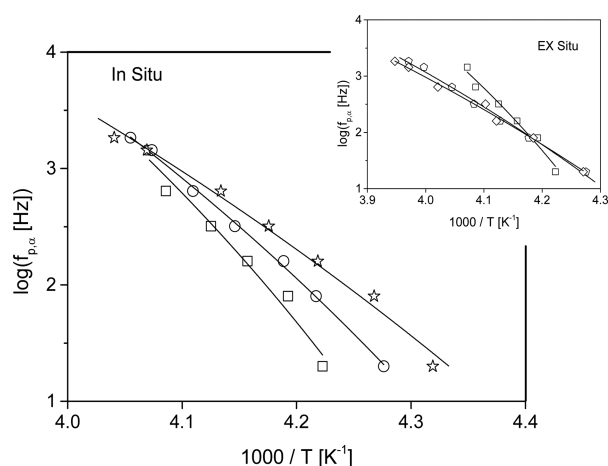
the glass transition (α relaxation) is difficult to be observed by dielectric spectroscopy. In these cases it is useful to present the dielectric spectra by the complex electric modulus $M^*(\omega)$ or/and complex conductivity $\sigma^*(\omega)$ where $M^*(\omega)$ is defined by

$$M^*(\omega) = M'(\omega) + iM''(\omega) = \frac{1}{\varepsilon^*} \qquad (3)$$

The complex conductivity is given by

$$\sigma^*(\omega) = \sigma'(\omega) + i\sigma''(\omega) = i\omega\varepsilon_0\varepsilon^*(\omega) \qquad (4)$$

ε_0 is the permittivity of free space.

Figure 10. Relaxation rate versus inverse temperature (relaxation map) as obtained from the ac-chip calorimetry measurements for the HPAE/Ka−DEA samples (*in situ*): squares, pure HPAE; circles, 2 wt % Ka−DEA; stars, 10 wt % Ka−DEA. The solid lines are fits of the VFT equation to the data. The inset shows the relaxation map the ac-chip calorimetry measurements for the HPAE/Ka−DCA samples (*ex situ*): squares, pure HPAE; pentagons, 5 wt % Ka−DCA; diamonds, 10 wt % Ka−DCA. Lines are fits of the VFT equation to the data.

Figure 11 displays the electric loss modulus $M''(\omega)$ of pure HPAE versus frequency and temperature in a 3D representa-
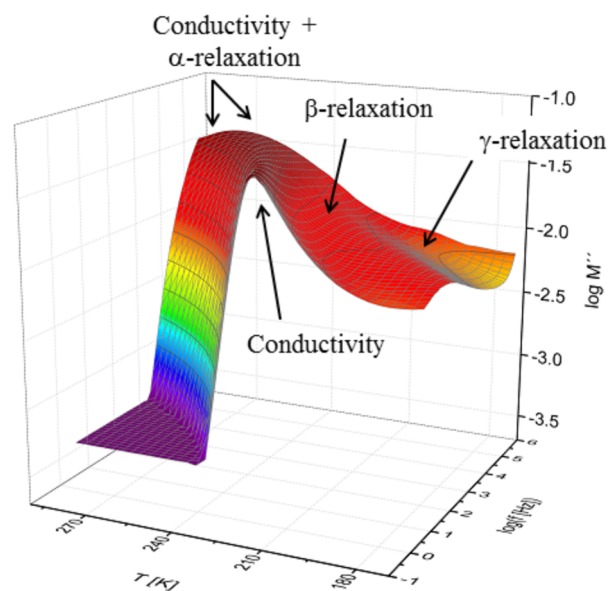

Figure 11. Imaginary part of the complex electric modulus of pure HPAE versus frequency and temperature in a 3D representation.

tion. In the modulus representation a conductivity contribution is converted into a peak.[62] Several dielectric active processes can be detected as peaks in the modulus representation. At low temperatures (high frequencies) a γ relaxation is observed. The γ relaxation is followed by the β relaxation with increasing temperature. At even higher temperatures (lower frequencies) the conductivity contribution is observed as a peak. This conductivity peak broadens for higher temperatures due to the underlying α relaxation. The upcoming part is arranged as follows: First, the γ relaxation is analyzed, and then the conductivity is considered in detail. The β relaxation cannot be

analyzed unambiguously because this process is strongly overlaid by the γ relaxation and the conductivity.

γ Relaxation. The γ relaxation is analyzed in the permittivity presentation. Figure 12 gives the dielectric loss for pure HPAE
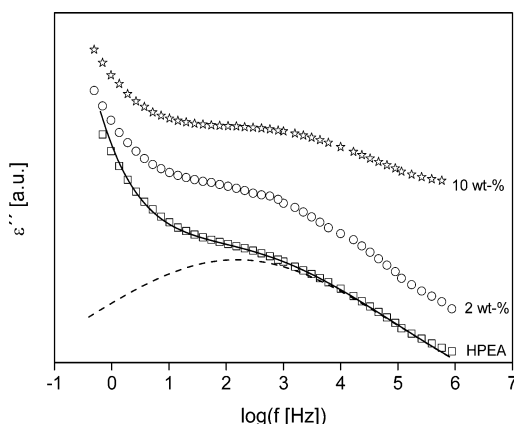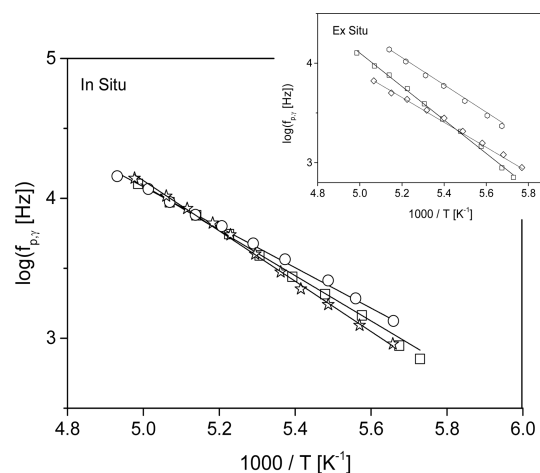

Figure 12. Dielectric loss ε'' versus frequency for the HPAE/Ka−DEA samples (*in situ*) at $T = 173$ K: squares, pure HPAE; circles, 2 wt % Ka−DEA; stars, 10 wt % Ka−DEA. The solid line is a fit of the HN function to the data of pure HPAE including a conductivity contribution. The dashed line indicates the contribution of the relaxation process.

and its nanocomposites with Ka−DEA (*in situ*) at $T = 173$ K. The γ relaxation is identified by a broad peak in the dielectric loss. From a molecular point of view, the γ relaxation is attributed to localized fluctuations of methyl and/or hydroxyl group rotation. These fluctuations could be coupled and/or also affected by both intra- and intermolecular hydrogen bonds, which are formed in these hyperbranched systems. For HPAE nanocomposites with 2 and 10 wt % of Ka−DEA, the γ relaxation broadens (see Figure 12). Assuming that the spectral shape of the γ relaxation can be described by a relaxation time spectra, one may conclude that the underlying molecular fluctuations become more heterogeneous in the nanocomposites. This is due to the polymer groups, which are in interaction with the nanoparticles and the segments, which have no interaction with the filler.

This relaxation process is further analyzed by fitting the empirical Havriliak−Negami (HN) function to the data. The HN function reads[63]

$$\varepsilon^*(f) = \varepsilon_\infty + \frac{\Delta\varepsilon}{\left(1 + \left(\frac{if}{f_0}\right)^\beta\right)^\gamma}$$

(5)

f_0 is a characteristic frequency related to the frequency of maximal loss f_p (relaxation rate), and ε_∞ describes the value of the real part ε' for $f \gg f_0$. β and γ are fractional parameters ($0 < \beta \leq 1$ and $0 < \beta\gamma \leq 1$) characterizing the shape of the relaxation time spectra. $\Delta\varepsilon$ denotes the dielectric strength. Conduction effects and contributions of other relaxation processes are treated in the usual way by adding a power law $\varepsilon''_{cond} = \sigma_0/[\omega^s\varepsilon_0]$ ($0 < s \leq 1$) to the dielectric loss. In the case of conduction, σ_0 is related to the specific dc conductivity of the sample. From the fit of the HN function the relaxation rate f_p is determined.[62] Figure 13 gives the temperature dependence of the relaxation rate $f_{p,\gamma}$ for γ relaxation in the relaxation map for

Figure 13. Relaxation map obtained from dielectric spectroscopy for the HPAE/Ka−DEA samples (*in situ*): squares, pure HPAE; circles, 2 wt % Ka−DEA; stars, 10 wt % Ka−DEA. The solid lines are fits of the Arrhenius equation to the data. The inset shows the relaxation map obtained from dielectric spectroscopy for the HPAE/Ka−DCA samples (*ex situ*): squares, pure HPAE; pentagons, 5 wt % Ka−DCA; diamonds, 10 wt % Ka−DCA. Lines are fits of the Arrhenius equation to the data.

the HPAE/Ka−DEA nanocomposites (*in situ*). Its temperature dependence can be described by an Arrhenius relation

$$f_p = f_\infty \exp\left(-\frac{E_{A,\gamma}}{k_B T}\right)$$

(6)

where k_B is the Boltzmann constant, $E_{A,\gamma}$ the activation energy, and f_∞ is the pre-exponential factor. The activation parameters for the γ relaxation of the different samples are given in Table 1.

For the HPAE/Ka−DEA samples, the estimated activation energies are more or less similar to that of neat HPAE. This is in agreement with some literature results. According to recent studies on linear polymers, for instance poly(ethylene oxide), confined within the galleries of layered silicates, the γ-relaxation was not affected by the confinement.[64] Moreover, quasielastic neutron scattering measurements on the hyperbranched poly(ester−amide) Hybrane showed that the γ-relaxation exhibited similar behavior in the pure polymer and under confinement.[32]

A recent BDS investigation of the confinement effect of layered MMT on the dynamics of three different generations of hyperbranched polyesters have reported that the γ-relaxation is significantly faster and with a lower activation energy than those of the pure polymer. This effect was identical for the three generations.[33] Here a similar behavior was observed for the samples prepared by the *ex situ* method (HPAE/Ka−DCA). In difference to the HPAE/Ka−DEA (*in situ*) nanocomposites, for the *ex situ* materials the activation energy decreases in confinement from ca. 30 to 25 kJ/mol. On a molecular level this could be understood by assuming that the system of hydrogen bonds due to the hydroxyl groups[27,28,40] is changed or partly disrupted for the HPAE/Ka−DCA samples due to the confinement and/or the presence of the nanoparticles. The differences in the structures of both kinds of different materials observed by the structural data (SAXS, TEM) are also reflected in its molecular dynamics as revealed by both the γ- and α-relaxation (see Figures 10 and 13).

Conductivity Contribution. Above the thermal glass transition the dielectric spectra are dominated conductivity contributions. Therefore, the conductivity formalism (see eq 4) should be employed to discuss the data. The frequency dependence of the real and imaginary part of the complex conductivity σ^* for pure HPAE and the nanocomposite is given in Figure 14a,b above T_g at $T = 257$ K. The conductivity spectra
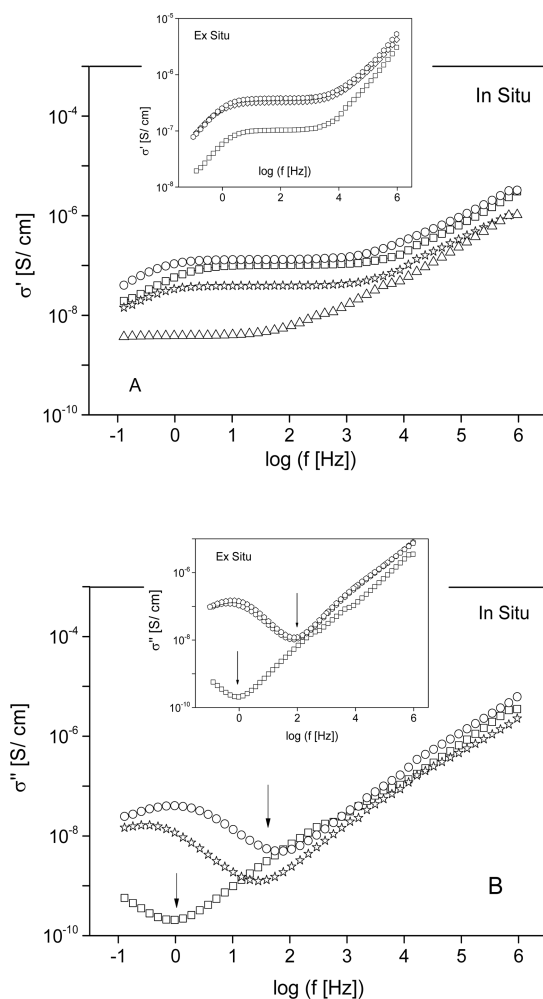
Figure 14. Real (A) and imaginary (B) part of the complex conductivity plotted versus frequency at $T = 257$ K: squares, pure HPAE; circles, 2 wt % Ka−DEA; stars, 10 wt % Ka−DEA. The insets show the same data for the HPAE/Ka−DCA samples (*ex situ*): squares, pure HPAE; pentagons, 5 wt % Ka−DCA; diamonds, 10 wt % Ka−DCA.

show the typical behavior expected for semiconducting polymeric materials. The real part σ' decreases with decreasing frequency with a power law down to a characteristic frequency f_σ, where a plateau value is reached. The plateau value corresponds to the dc conductivity.[65−69] The decrease in the real part of the complex conductivity at even lower frequencies is related to electrode and/or Maxwell−Wagner−Sillars polarization.[62] To discriminate between conduction and interfacial polarization effects, the imaginary part $\sigma''(f)$ of the complex conductivity is useful (see ref 70 and Figure 14b). The frequency corresponding to the minimum in $\sigma''(f)$ reflects the onset of interfacial polarization. The maximum in the $\sigma''(f)$ at a lower frequency is related to a fully developed interfacial polarization.[70] For the nanocomposites filled with Ka−DEA (*in*

situ samples), the value of the dc conductivity is more or less similar to unfilled HPAE (see Figure 14a). For the samples prepared by the *ex situ* method, the dc conductivity is higher than that for neat HPAE. This is related to the changed (enhanced close to T_g) segmental mobility revealed by the specific heat spectroscopy measurements (see inset Figure 10) induced by the nanofillers. Figure 14b reveals further that for all nanocomposites the onset of interfacial takes place at higher frequencies. This fact is indicated by the shift of the minimum in the imaginary part σ'' of the complex conductivity to higher frequencies (see Figure 14b). This enhanced interfacial polarization is related to Maxwell−Wagner−Sillars processes where the charge carriers were blocked at the nanofillers.

There are several models available in the literature to describe the frequency dependence of the real part of the complex conductivity like Dyre model where the conductivity is considered in the frame of hopping processes in a random free energy approach.[71] In a simplified way, the data can be approximated by the well-known Jonscher power law.[72]

$$\sigma'(f) = \sigma_{dc}[1 + (f/f_c)^n] \tag{7}$$

The exponent n is between 0.5 and 1. The critical frequency f_c characterizes the onset of the dispersion. By fitting the Jonscher equation to the data, both σ_{dc} and f_c are estimated.

Figure 15a depicts the dc conductivity σ_{dc} as a function of inverse temperature for the different nanocomposites. At the first glance, the non-Arrhenius temperature dependency of the dc conductivity relaxation reflects a certain coupling between the motion of the charge carriers and the fluctuations of the polymer segments yielding to glassy dynamics.[39] Like the relaxation rate of glassy dynamics, it can also be described by the Vogel−Fulcher−Tammann equation[29−31]

$$\log \sigma_{dc} = \log \sigma_\infty - \left(\frac{A}{T - T_0} \right) \tag{8}$$

where σ_∞ is the conductivity at infinite temperatures. At the first glance for both the HPAE/Ka−DEA and the HPAE−DCA nanocomposites, the temperature dependence of σ_{dc} varies in a similar manner as the relaxation rates estimated form specific heat spectroscopy (compare Figures 10 and 15a).

For a more detailed analysis of the temperature dependence of the dc conductivity, a derivative method is used.[73] This method is sensitive to the functional form of $\sigma_{dc}(T)$ irrespective of the prefactor. For a dependency according to the VFT equation one gets

$$\left[\frac{d(\log \sigma_{dc})}{dT} \right]^{-1/2} = A^{-1/2}(T - T_0) \tag{9}$$

Therefore, in a plot $[d(\log \sigma_{dc})/dT]^{-1/2}$ versus T, a VFT behavior shows up as a straight line (see Figure 15b). All experimental data can be well described by straight lines, which proves that the temperature dependence of the relaxation rates of both processes is VFT-like. A Vogel temperature T_0 for the conductivity can be estimated from both fits of the VFT equation to the corresponding data and by the derivative technique (see Table 2).

The estimated T_0 values for dc conductivity estimated by the direct fit of the VFT equation to the data and by the derivative technique are similar in the frame of the experimental error. For pure HPAE, the T_0 estimated form the dc conductivity is significantly lower than the value estimated by specific heat
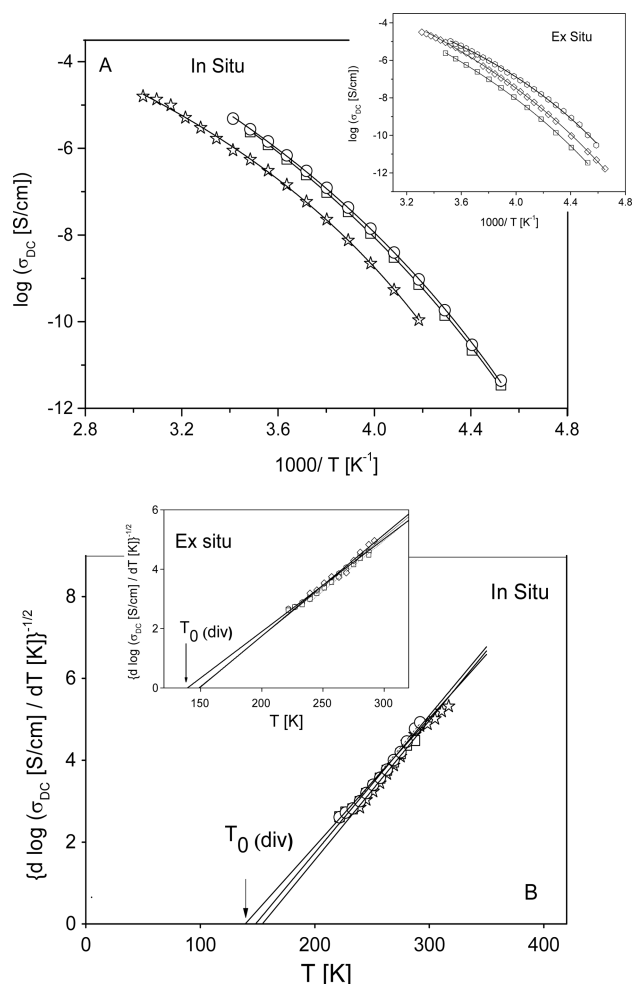
Figure 15. (A) Plot of dc conductivity σ_{dc} versus $1000/T$ for the HPAE/Ka−DEA samples (*in situ*): squares, pure HPAE; circles, 2 wt % Ka−DEA; stars, 10 wt % Ka−DEA. Lines are fits of the VFT equation to the data. The inset shows the temperature dependence of σ_{dc} for the HPAE/Ka−DCA samples (*ex situ*): squares, pure HPAE; pentagons, 5 wt % Ka−DCA; diamonds, 10 wt % Ka−DCA. Lines are fits of the VFT equation to the data. (B) Plot of $[d(\log \sigma_{dc})/dT]^{-1/2}$ versus temperature for the HPAE/Ka−DEA samples (*in situ*). The inset shows $[d(\log \sigma_{dc})/dT]^{-1/2}$ versus temperature for the HPAE/Ka−DCA samples (*ex situ*). The symbols are similar to those in part A. Lines are linear regressions to the corresponding data.

spectroscopy. This also reflected by quite different values of the fragility parameters (compare Tables 1 and 2). This result points to a certain decoupling of the temperature dependencies of the segmental dynamics and the conductivity. A corresponding behavior was also observed for other HBPs[4,61] and more general for polyelectrolytes.[74,75]

The differences in the Vogel temperatures found for segmental and conductivity can be discussed in two directions. First, it is known since a long time that the temperature dependence of the relaxation time of segmental and chain dynamics follow different VFT laws although theoretical treatments predicts the same temperature dependence with an identical Vogel temperature.[76−80] Such a behavior can be understood within the framework of the coupling model of Ngai.[81] More recently, this was intensively discussed by Sokolov and Schweitzer[82] where a decoupling index is defined and related to fragility of segmental dynamics. From a general point of view this decoupling seems to be related to the heterogeneity of glassy dynamics. The above considerations also apply for conductivity which is like chain dynamics a large scale motion.

Second, with regard to conductivity itself a decoupling index R_τ has been introduced by Angel.[83,84] It is defined as the ratio of the structural (segmental) relaxation time to the conductivity relaxation time. The decoupling index expresses how much faster the motion of the charge carriers are as expected from the segmental dynamics (α relaxation). Empirically it is given by $\log(R_\tau) = 14.3 + \log(\sigma_{dc}(T_g))$.[84] The estimated VFT parameters for conductivity are used to extrapolate σ_{dc} to the measured glass transition temperatures measured by DSC. Decoupling indexes between 2 and 3.5 have been estimated for pure HPEA and the different composites (see Table 2). This means that for the systems considered here the charge carriers are 2−3.5 orders of magnitude more mobile than expected from the segmental dynamics. Such high values of the decoupling index might be due to proton conduction In the presence of traces of water the carboxyl group is able to abstract a proton[85] which will lead to protonic conduction in these systems. A similar conduction mechanism was discussed for a different set of HBPs.[61]

With increasing concentration of the nanofiller, the difference between the Vogel temperatures of segmental dynamics and conductivity becomes smaller. This observation is in agreement with experimental results found for polyelectrolytes where this decoupling also becomes weaker with decreasing fragility of the segmental dynamics (see Table 1).[74]

The critical frequency f_c is related to the dc conductivity by the Barton−Nakajima−Namikawa relation (BNN)[86−88] $\sigma_{dc} \sim f_c$. In Figure 16, the dc conductivity σ_{dc} is plotted versus the critical frequency f_c (see eq 7) which characterizes the onset of the dispersion in charge transport. The data for pure HPAE as well as for all the composites follow a linear dependence and collapse into one chart. This is an expression of the empirical BNN relationship,[86−88] which is also fulfilled for the samples studied here independently of the structure of the prepared nanocomposite.

Table 2. VFT Parameters, Fragility Parameter D Estimated from the Conductivity, and Decoupling Index $\log(R_\tau)$ Estimated from the Conductivity of Pure HPAE and Its Nanocomposites

	sample	$\log(\sigma_\infty \text{ [S/cm]})$	A [K]	T_0 [K]	$T_{0(div)}$ [K]	D (conductivity)	$\log(R_\tau)$
	pure HPAE	1.93	1130	137	136	8.2	2.6
in situ	2 wt %	1.4	1004	143	149	7.1	2.5
	10 wt %	−0.33	736	163	154	4.5	2.1
ex situ	5 wt %	2.67	1185	143	141	8.5	2.1
	10 wt %	1.26	975	148	143	6.6	3.5
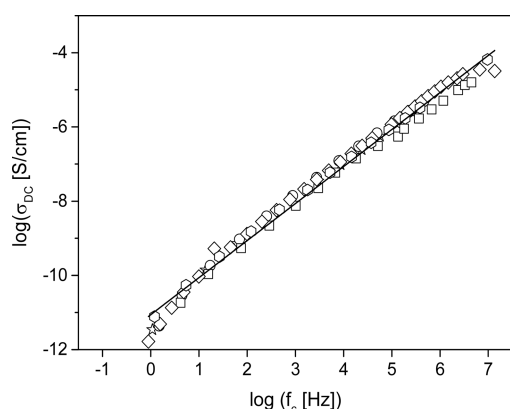
Figure 16. Plot of dc conductivity σ_{dc} versus the characteristic frequency f_c for pure HPAE and all nanocomposites: squares, pure HPAE; circles, 2 wt % Ka−DEA; stars, 10 wt % Ka−DEA; pentagons, 5 wt % Ka−DCA; diamonds, 10 wt % Ka−DCA. The solid line is a linear regression using all data points.

4. CONCLUSION

Nanocomposites based on hyperbranched polyamine ester and treated kaolinite were papered in two different ways. The first approach is an *ex situ* (solution-based) method, in which the prepared hyperbranched amine ester is inserted into the interlayers of the modified kaolinite. The second method is an *in situ* polymerization route. For the former method, the kaolinite has been modified by dodecylamine (DCA) and for the latter one by diethanolamine (DEA). From SAXS measurements, the Ka interlayer space increased from 0.71 to 3.6 nm^{-1} in Ka−DCA and to 1.1 nm^{-1} in Ka−DEA. SAXS and TEM investigations show that nanocomposites prepared by the *in situ* method have an intercalated morphology where *ex situ* preparation results in a more or less exfoliated structure.

By a combination of BDS and SHS, the relaxation properties of the nanocomposites were investigated in dependence on frequency and temperature. The results revealed that for all prepared samples the dielectric spectra are dominated on the lower frequency (higher temperature) side by conductivity contribution. The segmental motion related to the dynamic glass transition was found to be screened out by the conductivity contributions. The *in situ* HPAE/Ka−DEA samples have more or less a similar thermal glass temperature. Also, the localized molecular fluctuations (γ relaxation) is unaffected by the nanofiller. The specific heat spectroscopy investigations reveal that the dynamic glass transition changes from a more fragile behavior observed for pure HPEA to a stronger one for the nanocomposites.

For *ex situ* HPAE/Ka−DCA nanocomposites, the activation energies of γ relaxation for the nanocomposites were lower than the values found for the pure polymer. This is probably due to change or partly disrupted network of hydrogen bonds due to the confinement and/or the presences of the nanofiller. The confinement effect of the Ka−DCA nanofillers reduces the glass transition temperature and enhances, at the same time, the electrical conductivity of the polymer. Also, a systematic change of the dynamic glass transition estimated by ac-chip calorimetry was observed, which is in agreement with the behavior expected for a confined sample.

By comparing the temperature dependence of the dynamic glass transition measured with ac-chip calorimetry and that of the dc conductivity measured by dielectric spectroscopy, a decoupling in their temperature dependencies was found. With increasing concentration of the nanofiller, which results in a stronger glass-formation behavior, this decoupling becomes weaker. In the future, the reported results will be further studied and verified also for other systems of hyperbranched polymers but with the same nanofiller.

■ AUTHOR INFORMATION

Corresponding Author
*Tel +49 30/8104-3384; Fax +49 30/8104-1617; e-mail Andreas.Schoenhals@bam.de (A.S.).

Notes
The authors declare no competing financial interest.

■ REFERENCES

(1) Tomalia, D. A.; Baker, H.; Dewald, J.; Hall, M.; Kallos, G.; Martin, S.; Roeck, J.; Ryder, J.; Smith, P. *Polym. J.* **1985**, *17*, 117−132.
(2) Xu, Y.; Gao, C.; Kong, H.; Yan, D.; Luo, P.; Li, W.; Mai, Y. *Macromolecules* **2004**, *37*, 6264−6267.
(3) Voit, B. *J. Polym. Sci., Part A: Polym. Chem.* **2000**, *38*, 2505−2525.
(4) Adrjanowicz, K.; Kaminski, K.; Dulski, M.; Jasiurkowska-Delaporte, M.; Kolodziejczyk, K.; Jarek, M.; Bartkowiak, G.; Hawelek, L.; Jurga, S.; Paluch, M. *Macromolecules* **2014**, *47*, 5798−5807.
(5) Ratna, D.; Becker, O.; Krishnamurthy, R.; Simon, G.; Varley, R. *Polymer* **2003**, *44*, 7449−7457.
(6) Rodlert, M.; Plummer, C. J.; Grünbauer, H. J.; Månson, J. A. *Adv. Eng. Mater.* **2004**, *6*, 715−719.
(7) Rodlert, M.; Plummer, C. J.; Garamszegi, L.; Leterrier, Y.; Grünbauer, H. J.; Månson, J.-A. E. *Polymer* **2004**, *45*, 949−960.
(8) Plummer, C. J.; Rodlert, M.; Bucaille, J.-L.; Grünbauer, H. J.; Månson, J.-A. E. *Polymer* **2005**, *46*, 6543−6553.
(9) Alongi, J.; Monticelli, O.; Russo, S.; Voit, B. *J. Nanostruct. Polym. Nanocompos.* **2007**, *3*, 3−12.
(10) Chrissopoulou, K.; Altintzi, I.; Anastasiadis, S.; Giannelis, E.; Pitsikalis, M.; Hadjichristidis, N.; Theophilou, N. *Polymer* **2005**, *46*, 12440−12451.
(11) Chrissopoulou, K.; Altintzi, I.; Andrianaki, I.; Shemesh, R.; Retsos, H.; Giannelis, E.; Anastasiadis, S. *J. Polym. Sci., Part B: Polym. Phys.* **2008**, *46*, 2683−2695.
(12) Chrissopoulou, K.; Anastasiadis, S. *Eur. Polym. J.* **2011**, *47*, 600−613.
(13) Mott, C. *Catal. Today* **1988**, *2*, 199−208.
(14) Ke, Y.; Stroeve, P. *Polymer-Layered Silicate and Silica Nanocomposites*; Elsevier: Amsterdam, The Netherlands, 2005. p13.
(15) Bergaya, F.; Lagaly, G. *Dev. Clay Sci.* **2006**, *1*, 1−18.
(16) Essawy, H. *Colloid Polym. Sci.* **2008**, *286*, 795−803.
(17) Rehim, M. H. A.; Youssef, A. M.; Essawy, H. A. *Mater. Chem. Phys.* **2010**, *119*, 546−552.
(18) Letaief, S.; Detellier, C. *J. Therm. Anal. Calorim.* **2011**, *104*, 831−839.
(19) Xu, Y.; Brittain, W. J.; Xue, C.; Eby, R. K. *Polymer* **2004**, *45*, 3735−3746.
(20) Cortés, P.; Fraga, I.; Calventus, Y.; Román, F.; Hutchinson, J. M.; Ferrando, F. *Materials* **2014**, *7*, 1830−1849.
(21) Guessoum, M.; Nekkaa, S.; Fenouillot-Rimlinger, F.; Haddaoui, N. *Int. J. Polym. Sci.* **2012**, *2012*, 1−9.
(22) Gelade, E. T. F.; Goderis, B.; de Koster, C. G.; Meijerink, N.; van Benthem, R.; Fokkens, R.; Nibbering, N. M. M.; Mortensen, K. *Macromolecules* **2001**, *34*, 3552−3558.
(23) Froehling, P. *J. Polym. Sci., Part A: Polym. Chem.* **2004**, *42*, 3110−3115.
(24) Zagar, E.; Zigon, M.; Podzimek, S. *Polymer* **2006**, *47*, 166−175.
(25) Dritsas, G. S.; Karatasos, K.; Panayiotou, C. *Journal of Chromatography A* **2009**, *1216*, 8979−8985.
(26) Žagar, E.; Huskić, M.; Žigon, M. *Macromol. Chem. Phys.* **2007**, *208*, 1379−1387.

(27) Elrehim, M. A.; Said, S.; Ghoneim, A.; Turky, G. *Macromol. Symp.* **2007**, *254*, 1−8.

(28) Zhu, P. W.; Zheng, S.; Simon, G. *Macromol. Chem. Phys.* **2001**, *202*, 3008−3017.

(29) Vogel, H. *Phys. Z.* **1921**, *22*, 645−646.

(30) Fulcher, G. S. *J. Am. Ceram. Soc.* **1925**, *8*, 339−355.

(31) Tammann, G.; Hesse, W. *Zeitschrift für Anorganische und Allgemeine Chemie* **1926**, *156*, 245−257.

(32) Fotiadou, S.; Karageorgaki, C.; Chrissopoulou, K.; Karatasos, K.; Tanis, I.; Tragoudaras, D.; Frick, B.; Anastasiadis, S. *Macromolecules* **2013**, *46*, 2842−2855.

(33) Androulaki, K.; Chrissopoulou, K.; Prevosto, D.; Labardi, M.; Anastasiadis, S. H. *ACS Appl. Mater. Interfaces* **2015**, *7*, 12387−12398.

(34) Schönhals, A.; Schick, C.; Huth, H.; Frick, B.; Mayorova, M.; Zorn, R. *J. Non-Cryst. Solids* **2007**, *353*, 3853−3861.

(35) Schönhals, A.; Goering, H.; Schick, C.; Frick, B.; Zorn, R. *J. Non-Cryst. Solids* **2005**, *351*, 2668−2677.

(36) Ristić, S.; Mijović, J. *Polymer* **2008**, *49*, 4695−470.

(37) Mijović, J.; Ristic, S.; Kenny, J. *Macromolecules* **2007**, *40*, 5212−5221.

(38) Paluch, M.; Sekula, M.; Maslanka, S.; Manczyk, K.; Sulkowski, W. W.; Rozoska, S. J.; Ziolo, J. *J. Chem. Phys.* **2004**, *120*, 2020−2025.

(39) Dantras, E.; Dandurand, J.; Lacabanne, C.; Caminade, A. M.; Majoral, J. P. *Macromolecules* **2004**, *37*, 2812−2816.

(40) Turky, G.; Shaaban, S. S.; Schönhals, A. *J. Appl. Polym. Sci.* **2009**, *113*, 2477−2484.

(41) Kyritsis, A.; Raftopoulos, K.; Abdel Rehim, M.; Shabaan, S. S.; Ghoneim, A.; Turky, G. *Polymer* **2009**, *50*, 4039−4047.

(42) Malmstrom, E.; Liu, F.; Boyd, R. H.; Hult, A.; Gedde, U. W. *Polym. Bull.* **1994**, *32*, 679−685.

(43) Zhu, P. W.; Zheng, S.; Simon, G. *Macromol. Chem. Phys.* **2001**, *202*, 3008−3017.

(44) Huth, H.; Minakov, A.; Schick, C. *J. Polym. Sci., Part B: Polym. Phys.* **2006**, *44*, 2996−3005.

(45) Zhou, D. S.; Huth, H.; Gao, Y.; Xue, G.; Schick, C. *Macromolecules* **2008**, *41*, 7662−7666.

(46) Yin, H.; Schönhals, A. *Soft Matter* **2012**, *8*, 9132−9139.

(47) Yin, H.; Schönhals, A. *Polymer* **2013**, *54*, 2067−2070.

(48) Yan, D.; Gao, C.; Frey, H. *Dielectric Polymer Nanocomposites*; John Wiley & Sons: Hoboken, NJ, 2011; Vol. 8, p 118.

(49) Kremer, F.; Schönhals, A. Broadband dielectric measurement techniques. In *Broadband Dielectric Spectroscopy*; Kremer, F., Schönhals, A., Eds.; Springer: Berlin, Germany, 2002; p 35.

(50) Herwaaden, S.; Application note for Xsensor's calorimtere chips of XEN-39390 series.

(51) Gardolinski, J. E.; Peralta-Zamora, P.; Wypych, F. *J. Colloid Interface Sci.* **1999**, *211*, 137−141.

(52) Tunney, J. J.; Detellier, C. *Can. J. Chem.* **1997**, *75*, 1766−1772.

(53) Komori, Y.; Sugahara, Y.; Kuroda, K. *Appl. Clay Sci.* **1999**, *15*, 241−252.

(54) Zhang, S.; Lui, Q.; Cheng, H.; Li, X.; Zeng, F.; Frost, R. L. *J. Colloid Interface Sci.* **2014**, *430*, 345−350.

(55) Magaraphan, R.; Lilayuthalert, W.; Sirivat, A.; Schwank, J. W. *Compos. Sci. Technol.* **2001**, *61*, 1253−1264.

(56) Hu, X.-L.; Hou, G.-M.; Zhang, M.-Q.; Rong, M.-Z.; Ruan, W.-H.; Giannelis, E. P. *J. Mater. Chem.* **2012**, *22*, 18961−18967.

(57) Rehab, A.; Salahuddin, N. *Mater. Sci. Eng., A* **2005**, *399*, 368−376.

(58) Corcione, C. E.; Frigione, M. *Materials* **2012**, *5*, 2960−2980.

(59) Angell, C. A. *J. Res. Natl. Inst. Stand. Technol.* **1997**, *102*, 171−85.

(60) Angell, C. A. *Science* **1995**, *267*, 1924−1935.

(61) Sangoro, J.; Turky, G.; Abdel Rehim, M.; Iacob, C.; Naumov, S.; Ghoneim, A.; Kärger, J.; Kremer, F. *Macromolecules* **2009**, *42*, 1648−1651.

(62) Kremer, F.; Schönhals, A. Analysis of Dielectric Spectra. In *Broadband Dielectric Spectroscopy*; Kremer, F., Schönhals, A., Eds.; Springer: Berlin, Germany, 2002; p 59.

(63) Havriliak, S.; Negami, S. *Polymer* **1967**, *8*, 161. Havriliak, S.; Negami, S. *J. Polym. Sci., Part C: Polym. Symp.* **1966**, *14*, 99−117.

(64) Elmahdy, M. M.; Chrissopoulou, K.; Afratis, A.; Floudas, G.; Anastasiadis, S. H. *Macromolecules* **2006**, *39*, 5170−5173.

(65) Roling, B.; Happe, A.; Funke, K.; Ingram, M. D. *Phys. Rev. Lett.* **1997**, *78*, 2160−2163.

(66) Sidebottom, D. L. *Phys. Rev. Lett.* **1999**, *82*, 3653−3656.

(67) Zielniok, D.; Eckert, H.; Cramer, C. *Phys. Rev. Lett.* **2008**, *100*, 035901.

(68) MacDonald, J. R. *J. Non-Cryst. Solids* **1996**, *197*, 83−110.

(69) Iacob, C.; Sangoro, J.; Serghei, A.; Naumov, S.; Korth, Y.; Kärger, J.; Friedrich, C.; Kremer, F. *J. Chem. Phys.* **2008**, *129*, 234511.

(70) Serghei, A.; Tress, M.; Sangoro, J.; Kremer, F. *Phys. Rev. B: Condens. Matter Mater. Phys.* **2009**, *80*, 184301.

(71) Dyre, J. C. *J. Appl. Phys.* **1988**, *64*, 2456−2468.

(72) Jonscher, A. K. *Nature* **1977**, *267*, 673−679.

(73) Kremer, F.; Schönhals, A. The Scaling of the Dynamics of Glasses and Supercooled Liquids Spectra. In *Broadband Dielectric Spectroscopy*; Kremer, F., Schönhals, A., Eds.; Springer: Berlin, Germany, 2002; p 99.

(74) Wang, Y.; Fan, F.; Agapov, A. L.; Saito, T.; Yang, J.; Yu, X.; Hong, K.; Mays, J.; Sokolov, A. P. *Polymer* **2014**, *55*, 4067−4076.

(75) Wang, Y.; Agapov, A. L.; Fan, F.; Hong, K.; Yu, X.; Mays, J.; Sokolov, A. P. *Phys. Rev. Lett.* **2012**, *108*, 088303.

(76) Plazek, D. J.; O'Rourke, M. O. *J. Polym. Sci., Part A2* **1971**, *9*, 209.

(77) Plazek, D. J. *Polym. J.* **1980**, *12*, 43.

(78) Plazek, D. J.; Schlosser, E.; Schönhals, A.; Ngai, K. L. *J. Chem. Phys.* **1993**, *98*, 6488.

(79) Schönhals, A. *Macromolecules* **1993**, *26*, 1309−1312.

(80) Ding, Y.; Sokolov, A. P. *Macromolecules* **2006**, *39*, 3322−3326.

(81) Ngai, K. L.; Schönhals, A.; Schlosser, E. *Macromolecules* **1992**, *25*, 4915.

(82) Sokolov, A. P.; Schweizer, K. S. *Phys. Rev. Lett.* **2009**, *102*, 248301.

(83) Angell, C. A. *Annu. Rev. Phys. Chem.* **1992**, *43*, 693.

(84) Mizuno, F.; Belieres, J.-P.; Kuwata, N.; Pradel, A.; Ribes, M.; Angell, C. A. *J. Non-Cryst. Solids* **2006**, *352*, 5147.

(85) Fahmy, A.; Mix, R.; Schönhals, A.; Friedrich, J. F. *Plasma Processes Polym.* **2011**, *8*, 147−159.

(86) Barton, J. L. *Verres Refract* **1966**, *20*, 328.

(87) Nakajima, T. In 1971 Annual Report, Conference on Electrical Insulation and Dielectric Phenomena, 1972; pp 168−176.

(88) Namikawa, H. *J. Non-Cryst. Solids* **1975**, *18*, 173−195.